Neural tube morphogenesis in synthetic 3D microenvironments

Adrian Ranga[a,1], Mehmet Girgin[a], Andrea Meinhardt[b], Dominic Eberle[b], Massimiliano Caiazzo[a,2], Elly M. Tanaka[b], and Matthias P. Lutolf[a,c,3]

[a]Laboratory of Stem Cell Bioengineering, Institute of Bioengineering, School of Life Sciences and School of Engineering, Ecole Polytechnique Fédérale de Lausanne, 1015 Lausanne, Switzerland; [b]Center for Regenerative Therapies Dresden (CRTD), Technische Universität Dresden, 01307 Dresden, Germany; and [c]Institute of Chemical Sciences and Engineering, School of Basic Sciences, Ecole Polytechnique Fédérale de Lausanne, 1015 Lausanne, Switzerland

Edited by Brigid L. M. Hogan, Duke University Medical Center, Durham, NC, and approved August 5, 2016 (received for review March 2, 2016)

Three-dimensional organoid constructs serve as increasingly widespread in vitro models for development and disease modeling. Current approaches to recreate morphogenetic processes in vitro rely on poorly controllable and ill-defined matrices, thereby largely overlooking the contribution of biochemical and biophysical extracellular matrix (ECM) factors in promoting multicellular growth and reorganization. Here, we show how defined synthetic matrices can be used to explore the role of the ECM in the development of complex 3D neuroepithelial cysts that recapitulate key steps in early neurogenesis. We demonstrate how key ECM parameters are involved in specifying cytoskeleton-mediated symmetry-breaking events that ultimately lead to neural tube-like patterning along the dorsal–ventral (DV) axis. Such synthetic materials serve as valuable tools for studying the discrete action of extrinsic factors in organogenesis, and allow for the discovery of relationships between cytoskeletal mechanobiology and morphogenesis.

organoid | extracellular matrix | neural tube | development | embryonic stem cell

The earliest steps of development are characterized by complex cellular reorganization and differentiation within a 3D microenvironment (1). This 3D context allows for a dynamic spatial interplay between biochemical and biophysical signals, and governs the cellular rearrangements occurring during morphogenesis (2). Important fundamental mechanisms involved in early developmental events such as gastrulation and neurulation have classically been uncovered using in vivo cell lineage tracing and transplantation experiments (3, 4) combined with pharmacological and genetic perturbations using a range of model organisms such as *Xenopus*, zebrafish, chick, and mouse. Although such animal models have provided important insights, the complexity of the in vivo microenvironment even during the earliest developmental steps has proven a significant challenge in decoupling some of the key molecular mechanisms involved.

In vitro approaches have attempted to recapitulate key features of these processes, and it has now become possible to generate an increasing variety of self-organizing multicellular tissue constructs, termed organoids, that recreate features of such diverse organs as intestine, liver, brain, and spinal cord (5–8). Although important aspects of the 3D in vivo organization have been recapitulated in these organoid systems, such studies have been exclusively performed in Matrigel, a poorly defined, largely proteinaceous mixture whose properties cannot be readily modulated. As such, the interactions between cells and this ECM have remained poorly characterized and have proven to be a major challenge to understanding the underlying regulatory mechanisms governing morphogenesis.

The advent of highly tunable synthetic extracellular matrices has allowed for increasing flexibility in probing the role of ECM-derived factors in specifying stem cell fate (9–11). By breaking down the associated physiological complexity into an experimentally amenable number of distinct interactions, such ECM analogs bridge the gap between traditional 2D cell culture methods (i.e., plastic culture dishes) and labor-intensive animal models, while avoiding the pitfalls of naturally derived 3D matrices such as Matrigel and collagen.

In recent years, several studies have attempted to fully exploit the modular possibilities of synthetic materials to systematically deconstruct the in vivo niche using high-throughput approaches (12, 13). Although these studies have heralded the potential of robotically arrayed, rationally designed 3D microenvironmental manipulation of the extracellular microenvironment, they have not tackled the problem of multicellular morphogenesis. Indeed, the development of synthetic materials design strategies, notably based on poly(ethylene glycol) (PEG) hydrogels, have allowed for the generation of modular ECM component libraries serving as molecular gel building blocks (14, 15). The components of these libraries can be assembled independently to create microenvironments with nearly infinite combinatorial possibilities, resulting in unique experimental conditions where matrix stiffness, degradability, and tethered and soluble factors can all be assessed in an unbiased and highly systematic manner. To explore such a large materials parameter space, we have developed a high-throughput approach based on a combination of liquid-handling automation, high-throughput microscopy, and customized bioinformatics tools, which has allowed us to perform discrete combinatorial modulation of the 3D cell microenvironment in multifactorial and highly parallelized fashion (16). Although we have illustrated the possibilities of such a system by deploying

Significance

In vitro organoids have become widely used model systems in basic research and for therapeutic applications due to their ability to recapitulate key elements of in vivo form and function. However, their full potential remains unfulfilled as a result of the poorly defined matrices in which they are grown. Here, we use modular synthetic 3D matrices to show that early neural morphogenesis can be precisely controlled by the extracellular microenvironment. Our approach is broadly applicable to gain a broader understanding of the multifactorial 3D cell–matrix interactions that coordinate multicellular growth and differentiation, and opens up avenues to discover and dissect the unique microenvironments that control morphogenesis in various organoid systems.

Author contributions: A.R., E.M.T., and M.P.L. designed research; A.R., M.G., D.E., and M.C. performed research; A.M. and D.E. contributed new reagents/analytic tools; A.R., E.M.T., and M.P.L. analyzed data; and A.R., E.M.T., and M.P.L. wrote the paper.

The authors declare no conflict of interest.

This article is a PNAS Direct Submission.

Freely available online through the PNAS open access option.

[1]Present address: Department of Mechanical Engineering, Biomechanics Section, KU Leuven, 3001 Leuven, Belgium.

[2]Present address: Institute of Genetics and Biophysics, "A. Buzzati-Traverso," Consiglio Nazionale delle Ricerche, 80131 Naples, Italy.

[3]To whom correspondence should be addressed. Email: matthias.lutolf@epfl.ch.

This article contains supporting information online at www.pnas.org/lookup/suppl/doi:10.1073/pnas.1603529113/-/DCSupplemental.

it to elucidate mechanisms of self-renewal involved in mouse embryonic stem cells (ESCs), and others have shown how such modularity can begin to elucidate elements of apicobasal polarity in epithelial Madin–Darby canine kidney (MDCK) cysts (17), it has as-yet not been possible to recreate complex, patterned 3D multicellular structures in such synthetic microenvironments, particularly in the context of neural development.

To begin to understand how molecular signals and the extracellular microenvironment coordinate to form early structures of the central nervous system (CNS), we have begun to generate organoids with defining features of developing spinal cord (8). Our previous work with Matrigel has shown that single mouse ESCs could form apical–basal neuroepithelial cysts containing single lumens (8), and that retinoic acid (RA) could induce such cysts to yield patterning along a dorsal–ventral (DV) axis recalling the spatial organization found in the developing neural tube. Although some studies with synthetic PEG matrices have suggested that adhesion ligands play an important role in establishing apical–basal polarity in model systems of epithelial morphogenesis (18), it has remained unresolved which aspects of Matrigel contribute to this spatial organization, and in particular the role of extracellular microenvironment in establishing complex morphogenesis. Here, we exploit our synthetic materials library to investigate conditions leading to optimal early neural commitment events in an ESC-derived model of neural tube patterning. The use of a high-throughput approach for automated hydrogel generation and systems-level analysis allows us to first disentangle the contributions of biochemical and physical components of the microenvironment in the specification of 3D neurogenesis. We then investigate the role of the ECM in determining subsequent CNS patterning, focusing more particularly on the relationship between apical–basal polarity and DV patterning. Additionally, we use this neural tube construct to investigate how the modulation of cytoskeleton dynamics affects patterning events, and provide a proof of principle of the use of such a defined model system to study the involvement of cardinal developmental pathways in defining early symmetry-breaking events in the nervous system. This approach provides a versatile in vitro tool that can decouple key factors in CNS development, as well as insights into the potentially disruptive role of the ECM in CNS pathologies.

Results

Deconstructing and Reconstructing Matrigel. To rapidly and systematically assess the role of a wide variety of potential extracellular modulators of neuroepithelial differentiation and morphogenesis in Matrigel, we made use of a PEG-based engineered hydrogel platform composed of a library of molecular building blocks that could be independently mixed and then cross-linked in the presence of cells, to form a diversity of 3D microenvironments with distinct and nearly independently controllable properties (16) (Fig. 1). The physical properties of this synthetic matrix could be specified by altering the polymer content, and the peptide domain linked to the PEG backbone

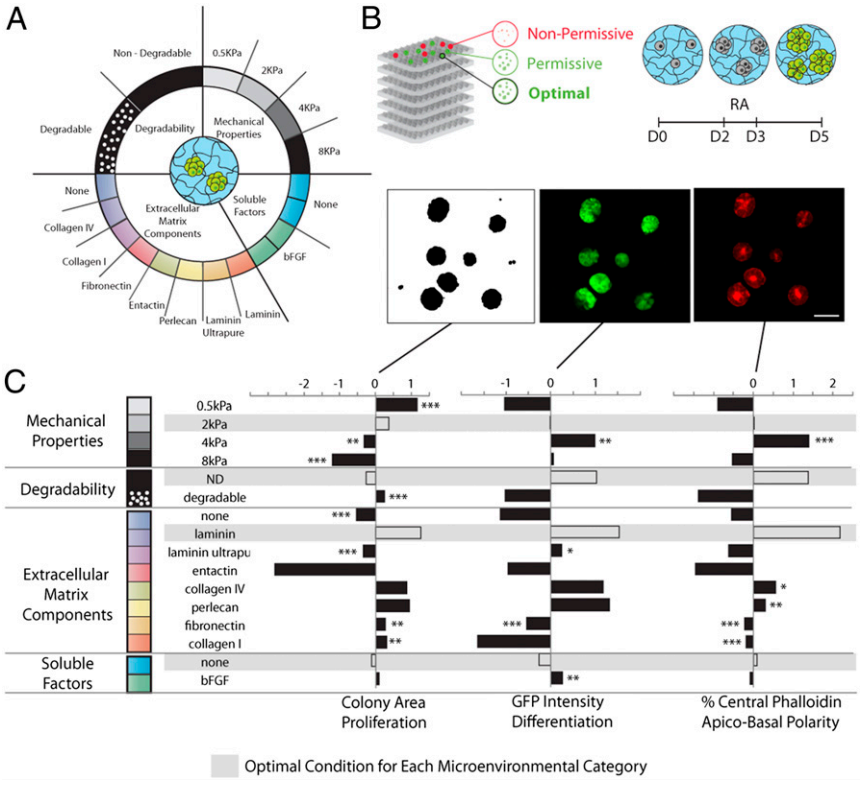

Fig. 1. A library of molecular building blocks are mixed and cross-linked in situ to form cell-containing 3D hydrogels with independently controllable mechanical and biochemical properties (*A*). Colonies are differentiated over 5 d, with RA treatment at D2–3. A Sox1-GFP ESC reporter line is used to visualize neural differentiation. Apical–basal polarity is evaluated based on the presence of a characteristic actomyosin contractile ring upon phalloidin staining of the actin cytoskeleton. These markers, along with colony size as an indicator of proliferation, are assessed using an automated imaging and image analysis pipeline (*B*). (Scale bar: 50 μm.) Systematic investigation of the role of the microenvironment is performed by GLMs, yielding the relative contribution of each factor; statistical analysis identifies the significance of the change with respect to the condition in white for every category (*C*). Data are shown normalized and centered across the experiment, where a result of 0 indicates a value that corresponds to the mean for the entire experiment. A "signature of differentiation" consisting of a compromise optimal condition within each category across the readouts (proliferation, differentiation, and apical–basal polarity) is thus identified and highlighted in gray.

could be altered to be either sensitive or completely insensitive to degradation by matrix metalloproteinases (MMP) (16). To determine the key bioactive elements of Matrigel involved in morphogenesis, we assessed known components of Matrigel such as collagen IV, entactin, laminin-111 (in pure and entactin-rich forms), and perlecan (Fig. 1*A*). Additionally, we selected ECM components that have not been reported to feature significantly in its composition, such as fibronectin and collagen I. We also included the growth factor bFGF, which has been reported to enhance early in vitro neuromesodermal development (19). To combine these elements, we implemented a fully factorial method based on the automatic liquid handling of hydrogel precursors (16) (Fig. 1*B*). In the most permissive conditions, colonies formed within 2 d and continued growing into cyst-like structures (Fig. 1*B*). Three key markers involved in differentiation were assessed at day 5 (D5): proliferation, neural identity, and apical–basal polarity (Fig. 1*C*).

Role of Individual ECM Components on Single ESC Fate and Early Morphogenesis. To assess the role of these combinatorially arrayed factors, we imaged the array plates and performed image analysis on each well, corresponding to a unique microenvironmental condition. The data generated were then analyzed using a generalized linear models (GLMs)-based framework, where the role of each microenvironmental factor could be deconvolved (16).

Our microenvironment screening revealed a significant role of the physical matrix properties in modulating neuroepithelial fate (Fig. 1*C*): an intermediate stiffness ($E = 2$ and 4 kPa) promoted this process, whereas softer and stiffer conditions ($E = 0.5$ kPa and $E = 12$ kPa) resulted in down-regulation of Sox1-GFP expression. An intermediate stiffness was required for achieving optimal apical–basal polarity. In contrast, the softest matrix promoted the most proliferation, indicating that, in this system, growth and differentiation might be uncoupled processes.

One of the more surprising extrinsic effectors of neuroepithelial differentiation uncovered in this screen was gel susceptibility to degradation by MMPs. In matrices that could not be degraded, we observed a significantly higher Sox1-GFP intensity than in degradable matrices (Fig. 1*C*). As with stiffness, apical–basal polarity correlated with Sox1-GFP expression and was inversely proportional to colony size.

Of the ECM proteins tested, laminin was the most positive modulator of all three readouts. Similarly, but to a lesser degree, collagen IV and perlecan, all components of Matrigel, could elicit a favorable response across readouts. ESCs in PEG matrices that did not incorporate any ECM proteins proliferated and differentiated to a significantly lesser extent than those in favorable ECM conditions, suggesting that a 3D microenvironment is an absolute requirement for morphogenesis, but that additional factors are required to achieve optimal neuroepithelial differentiation. bFGF had only a minor effect on proliferation, and no significant influence on either apical–basal polarity or neuroepithelial identity. This suggests that, in a 3D context, its effect could be dispensable, or secreted and maintained by the colonies themselves in an autocrine fashion, or mediated by paracrine effects from neighboring colonies.

To further explore our multidimensional dataset, we represented the relationships between readouts for each individual condition (Fig. S1). It was possible to verify that our global GLM analysis indeed correlated with individual identified optimal conditions. To exploit additional morphometric features of our data, we performed clustering analysis (Fig. S2), based on the three key readouts but, additionally, on total number of colonies per well, colony eccentricity, and solidity. This analysis led to the identification of characteristic colony identities, which could then be tracked back to their initiating microenvironments. We could also identify the microenvironmental conditions that caused differences between adjacent clusters as well as identify new phenotypes.

Neuroepithelial Colonies in Synthetic Matrices Are More Homogenous and Polarized Than in Matrigel. Matrigel is the gold standard matrix for in vitro morphogenesis studies. We therefore compared the development of neuroepithelial colonies grown in our optimal synthetic matrix to those in Matrigel. One of the main features of cells in Matrigel is the appearance of highly heterogeneous colonies, both in morphology and size (Fig. 2). Indeed, starting from the first cell divisions, Matrigel-grown colonies exhibit differing phenotypes, with mixed epithelial and mesenchymal phenotypes observed (Fig. 2*A*). In contrast, colonies in optimized PEG matrices develop as smooth, spherical entities (Fig. 2*B*). As colonies grow in Matrigel, merging between colonies is frequently evidenced (Fig. 2*C*), whereas in PEG gels colonies remain distinctly separated even when adjacent (Fig. 2*D*). Together, the differences in material properties and composition between PEG and Matrigel result in very different outcomes: Matrigel leads to more heterogeneous colony size and morphology compared with PEG (Fig. 2 *E* and *F*), and a significantly

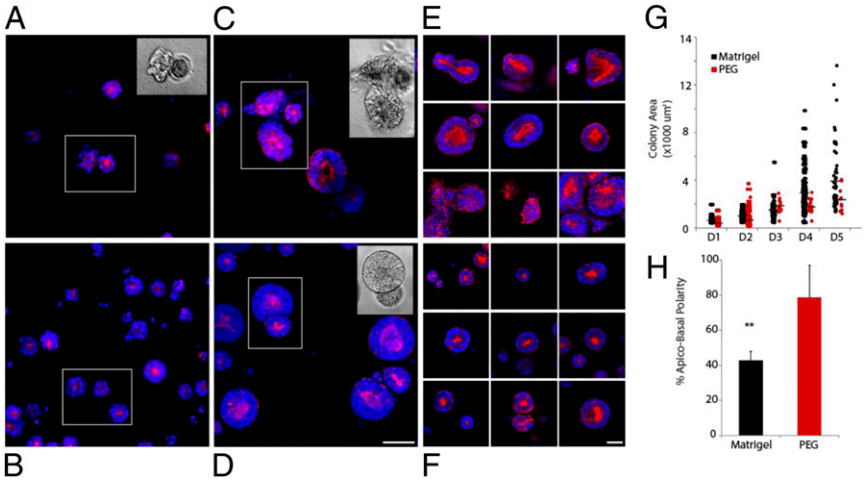

Fig. 2. Neuroepithelial cysts in Matrigel and optimal PEG hydrogel condition at D2 (*A* and *B*, respectively) and D5 (*C* and *D*), with additional representative colonies at D5 (*E* and *F*). Colony area was quantified for both conditions within a representative time series (*G*), with a comparison of ensuing apical–basal polarity evaluated at D5 (*H*). (Scale bars: 50 μm.) $^{**}P < 0.01$.

higher proportion of cysts with apical–basal polarity can be achieved in PEG (Fig. 2*H*). Even colonies that remain as single units and exhibit epithelial characteristics present a wide range of organization and morphologies. Notably, over time, colony growth is limited in PEG, whereas in Matrigel it continues with little physical constraint, with a much wider distribution in colony size (Fig. 2*G*).

DV Patterning and Neural Tube Architecture Can Be Achieved in Optimal Synthetic Matrices. To determine whether our synthetic matrix could support further differentiation and development, we grew single ESCs for 7 d, corresponding to embryonic day (E) 10.5, when the neural tube has formed to the extent that DV patterning and cellular rearrangements are evidenced.

A number of key markers of DV patterning seen in vivo could be recapitulated in our synthetic 3D culture system. In particular, sonic hedgehog (Shh) was frequently seen to localize asymmetrically, at the lateral edge of the cysts, in a configuration analogous to the floor plate of the neural tube (Fig. 3*A*). In all cases, Sox1-GFP expression was excluded from the Shh^+ region, as would be expected from the exclusion of GFP fluorescence from the midline of the Sox1-GFP embryo at E11.5 (20). Other key architectural features of the neural tube corresponding to this stage of in vivo development were also recapitulated: Nkx-6.1, a transcription factor induced by Shh, which acts to restrict the generation of motor neurons to the appropriate region of the neural tube, as well as $Olig2^+$ motor neuron progenitors were evidenced within the cyst, whereas Isl1/2 mature motor neurons were seen at the periphery, at the same level as the motor neuron progenitors. It was also possible to identify $Pax3^+$ colonies at the opposite end of the Shh location, demonstrating that these cysts achieve not only ventral but also dorsal patterning (Fig. 3*B*).

Key Morphogenetic Features Follow Specific Temporal Dynamics. Having defined an optimal matrix for cyst formation and then demonstrated that a patterned neural tube-like construct could be formed in such a matrix, we next thought to shed light on the developmental dynamics of this process. As in Matrigel (8), apical–basal polarity was established very early, after the first few cell divisions (Fig. 3*C*). This first morphogenetic process was evidenced in the majority of cysts after 2 d, indicating that the ECM has a direct and immediate influence on cells derived from the first cell divisions. Time-lapse microscopy revealed this process to be highly dynamic, with significant cytoskeletal rearrangement that stabilized into a central actin ring only by the third day of culture (Movies S1–S8). Neural fate, as assessed by

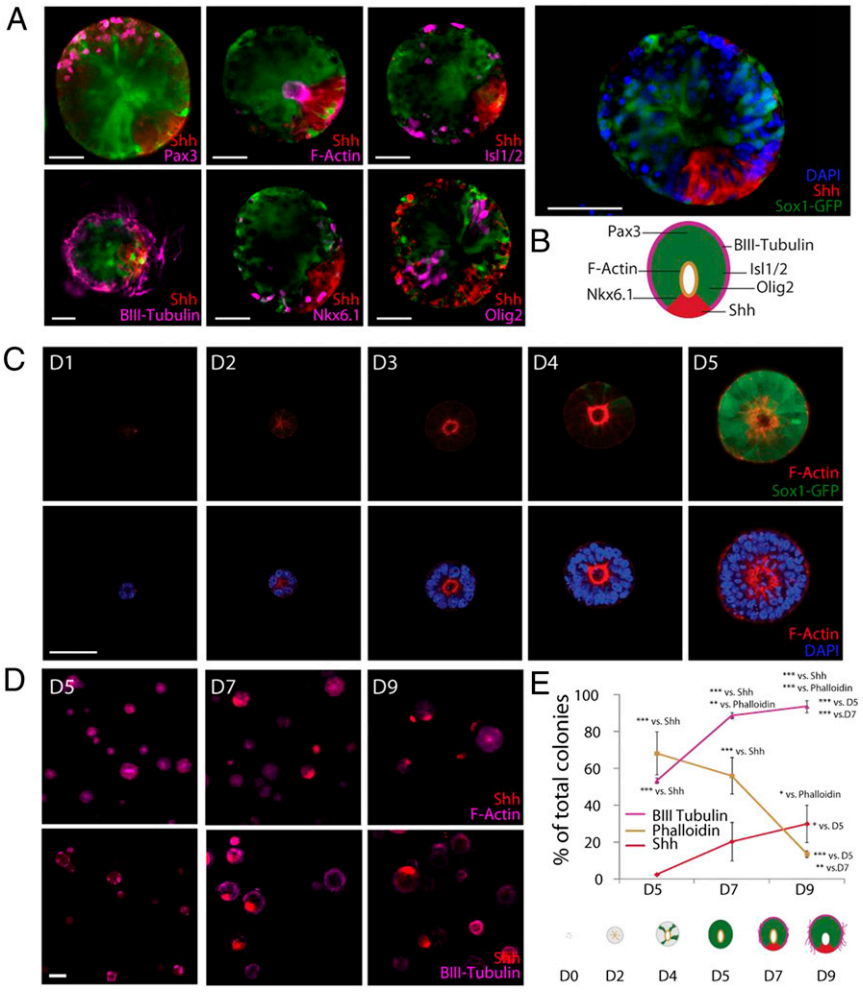

Fig. 3. Cyst identity is characterized by markers of DV patterning in optimal synthetic matrix conditions (*A*). Cyst patterning exhibits key features of neural tube architecture, including floor plate (Shh), progenitor motor neuron (Olig2), motor neuron (Isl1/2), postmitotic neuron (βIII-tubulin), as well as ventral (Nkx6.1) and dorsal (Pax3) positional identities, represented schematically (*B*). Representative images of a time series with Sox1-GFP expression and F-Actin staining (D1 to D5) (*C*), and with Shh, F-Actin, and βIII-tubulin staining (D5 to D9) (*D*). Quantification of key events in morphogenetic patterning in 3D (*E*). (Scale bars: *A* and *C*, 50 μm; *D*, 100 μm.) $***P < 0.001$, $**P < 0.01$, $*P < 0.05$.

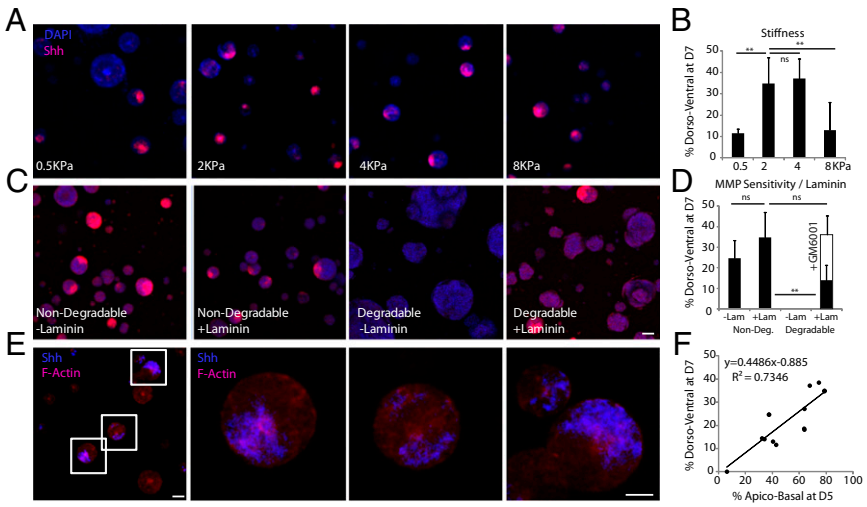

Fig. 4. Representative images of Shh-stained cysts in nondegradable matrices of various stiffness (*A*) and in 2-kPa matrices of various degradability and laminin compositions (*B*) with corresponding quantification of DV patterning efficiency for each condition (*C* and *D*). F-actin and Shh costaining of cysts in nondegradable, 2-kPa, laminin-containing matrix, indicating apical–basal and DV patterning, respectively, with higher magnification images (*E*). The relationship between apical–basal polarity at D5 and DV patterning at D7 is quantified for all tested conditions (*F*). [Scale bars: *A*, *C*, and *E* (*Left*), 100 μm; *E* (*Right*), 50 μm.] $^{**}P < 0.01$.

Sox1-GFP, was evidenced at a much later time point than the establishment of apical–basal polarity (at D4), indicating that the first steps of morphogenesis precede the specification of neural fate (Fig. 3*C*).

To understand how the later architectural features of the in vitro neural tube-like structures develop and progress over time, we tracked three markers as surrogates for morphogenesis: cortical actin, localized Shh, and βIII-tubulin as measures of apical–basal polarity, DV polarity, and mature neurogenesis, respectively (Fig. 3*D*). Apical–basal polarity, established in the large majority of cysts at D5, subsequently decreased over time, most dramatically between D7 and D9, suggesting that the F-actin network stabilization and associated forces are no longer required once cyst architecture has been established. Conversely, postmitotic neurons appeared at the periphery at D5, and completely enveloped and projected from the cyst by D9. Finally, DV patterning was not evidenced to any significant extent at D5, appearing at D7, and increasing to D9.

Matrix Stiffness, Degradability, and ECM Composition Influence Patterning Efficiency. Having characterized the development of neural tube-like constructs in the baseline optimal matrix derived from our screen, we next thought to independently modulate matrix properties to determine how the microenvironment affected later morphogenesis. A matrix characterized by intermediate stiffness ($E = 2$ kPa and $E = 4$ kPa) led to the most efficient DV patterning (Fig. 4 *A* and *B*), whereas both the softest ($E = 0.5$ kPa) and stiffest ($E = 12$ kPa) matrices exhibited the lowest proportion of DV patterning. The effect of stiffness on DV patterning closely mapped to our findings on optimal stiffness for apical–basal patterning, suggesting that these two morphogenetic events are linked. Interestingly, the stiffness of Matrigel and laminin–entactin gels is significantly lower than our optimal materials, thereby indicating that the mechanism of morphogenesis in these naturally derived matrices could be different from that within our synthetic gels. Our results suggest that the high ECM content of Matrigel and laminin–entactin could override stiffness-mediated effects, and that our synthetic matrices allow us to more clearly disentangle these orthogonal effects by allowing for the independent modulation of stiffness and ECM content within a biologically neutral background.

The importance of the extracellular milieu in specifying morphogenesis is further underscored by our results when manipulating matrix MMP sensitivity (Fig. 4 *C* and *D*). Colonies in nondegradable matrices had a characteristic round morphology, suggesting that isotropic growth could be required for the establishment of a polarity (Movies S1–S4). The formation of apical–basal polarity in nondegradable matrices led to correspondingly high DV patterning proportions. Even in a nondegradable matrix devoid of any instructive ECM cues, providing dimensionality alone at the optimal intermediate stiffness was sufficient to allow for the establishment of DV polarity. The addition of laminin also enhanced the establishment of DV patterning. In contrast, cells in MMP-sensitive matrices devoid of additional factors allowed for no DV patterning whatsoever, whereas the addition of laminin led to a minimal percentage of cyst patterning. In such matrices, colonies maintained at least some measure of Sox1-GFP but did not develop into characteristic spherical neuroepithelial colonies (Movies S5–S8). This suggests that the physical characteristics of the matrix are involved in dictating fate choice by coordinating cell shape and invasion characteristics, and that permissive matrices may in fact promote loss of epithelial characteristics.

To ascertain that aberrant morphogenesis was indeed mediated by local proteolytic degradation of the matrix, we treated degradable matrices with a broadband MMP inhibitor (GM6001). MMP inhibition resulted in not only a complete recovery of a round colony phenotype identical to that seen in MMP-insensitive matrices but also a concomitant enhancement in DV patterning.

To explore the relationship between early (apical–basal) and later (dorsal–ventral) morphogenesis, we examined the efficiency of apical–basal polarity at D5 vs. that of DV patterning at D7 for each of the conditions above (Fig. 4 *E* and *F*). Indeed, when all conditions were represented together, a linear correlation clearly emerged ($R^2 = 0.73$), where, irrespective of conditions, one-half of the proportion of all apicobasally polarized colonies at D5 became DV patterned at D7. Coimmunostaining for both apical–basal and DV at D7 showed that all cysts with localized Shh expression were also apicobasally polarized (Fig. 4*E*), indicating that apical–basal polarity was required for DV patterning.

Proliferation, Tissue Structure, and ECM Deposition is Regulated by Matrix Properties. We further assessed how proliferation and apoptosis were involved in these morphogenic events. In our

baseline matrix, apoptotic cells were evidenced at the center of polarized cysts at D3, and were surrounded by proliferating EdU-positive cells, suggesting that apical–basal polarization was initiated by apical apoptosis (Fig. 5). By D5, proliferation was reduced in most cysts, whereas, at D7, most cysts exhibited an outer ring of apoptotic cells, while maintaining proliferating EdU$^+$ cells in the inner core. Notably, all Shh$^+$ regions were nonproliferating, consistent with reports showing that cells in the developing neural tube are specified to floor plate identity by reducing their ability to proliferate and by blocking their ability to differentiate into neuroblasts. Proliferation and apoptosis at these key time points were also evidenced in other matrix conditions (Fig. S3). These data suggest that matrix properties not only regulate the dynamics of cell fate changes, but also proliferation and apoptosis, and that an optimal matrix encodes the correct balance between these two mechanisms to promote morphogenesis.

To address how neural and epithelial markers are influenced by the microenvironment, N-Cadherin and E-Cadherin expression was assessed over time in gels of varying stiffness and MMP sensitivities (Fig. 5*B* and Figs. S4 and S5). N-Cad was expressed even at low levels at all stages of differentiation, with apical–basal polarity of N-Cad observed starting only after D3. Conversely, all cysts were E-Cad$^+$ at D3, with E-Cad expression markedly decreasing in time. Notably, in optimal matrix conditions, E-Cad was apicobasally polarized at D3, with some cysts maintaining E-Cad$^+$ domains to D7 (Fig. 5*B*). N-Cad/E-Cad composition changed as a function of the microenvironment, with higher incidence of apicobasally polarized, N-Cad$^+$ cysts observed in nondegradable matrices. This suggests that the matrix can influence the epithelial-to-neural switch, particularly in sustaining apical–basal polarization of N-Cad, which seems to be required for further DV patterning.

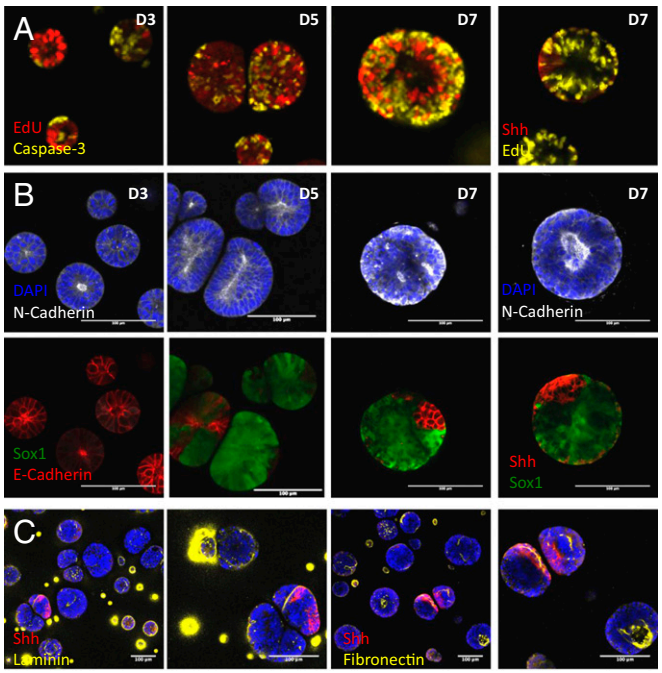

Fig. 5. Characterization of proliferation/apoptosis, neural/epithelial identity, and ECM production in standard 2KPa MMP-insensitive synthetic matrix. (*A*) Cysts are highly proliferative at D3, followed by gradual apoptosis mainly at the basal aspect. Proliferation is absent in the Shh region. (*B*) N-Cadherin is apically-basally polarized in cysts which undergo morphogenesis. E-Cadherin is present in all cysts at D3 and is rapidly lost by D5. E-Cad is still present in some cysts up to D7. (*C*) Cysts produce laminin and fibronectin, frequently localized at the Shh polarized and apical region of the cyst. (Scale bar: 100 μm.)

To determine whether these cysts produced their own basement membrane, we assessed two key ECM components of the basement membrane in our standard RA-pulse differentiation protocol. Intriguingly, in an ECM-free matrix, both fibronectin and laminin were present in most cysts (Fig. 5*C* and Fig. S6). Similarly, in standard laminin-containing matrices, both ECM proteins were observed, at similar intensities and frequency as in the laminin-free matrices, suggesting that the addition of exogeneous laminin at the start of differentiation was not directly involved in enhanced matrix production. In both conditions, ECM proteins were mainly detected on the surface of the cysts, and in the lumen of apicobasally polarized cysts. Notably, in Shh patterned cysts, we observed that ECM deposition was mainly located at the floor plate region, suggesting a potential relationship between ECM deposition and patterning.

Patterning Efficiency Can Be Modulated via RhoA/Rho Kinase Pathway. Having recognized the significance of the cytoskeletal rearrangement in initiating morphogenesis and having established its role in later DV patterning, we next examined how modulating cellular contractility affected morphogenesis of the engineered neural tube constructs. The establishment of apical–basal polarity through apical constriction is mediated by actomyosin activity (21) and is regulated by signaling through RhoA, its effector Rho kinase (ROCK), and myosin light-chain kinase (MLCK). Here, we treated our cultures with lysophosphatidic acid (LPA), an activator of Rho, and ML7, an inhibitor of MLCK, to probe the effect of changes in cytoskeletal contractility on patterning. Notably, we restricted treatment only to the early time point between D2 and D3 where polarity and patterning were initiated, concomitant with RA treatment.

Directly after LPA treatment, a large proportion of cysts did not reorganize their cytoskeleton into contractile rings (Fig. 6*A*) and demonstrated an inverted polarity (Fig. 6*B*). This effect was recovered to some extent by D5; however, few of the cysts that could recover apical–basal polarity maintained it to D7. As a direct consequence, the establishment of DV polarity was completely abrogated (Fig. 6*C*), demonstrating that hyperactivation of Rho could destabilize cytoskeletal rearrangements and completely perturb later patterning. Conversely, inhibition of MLCK II by ML7 had the opposite effect: reducing cytoskeleton contractility allowed for enhanced cellular rearrangements, with more prominent rings formed even at D3 (Fig. 6*A*), resulting in a significant enhancement of DV patterning (Fig. 6*C*).

Taking advantage of our ability to modulate the stiffness of the matrix, we investigated whether the mechanical forces extrinsically imposed by the matrix could work cooperatively with intrinsic modulators of cytoskeleton contractility to effect changes in morphogenesis. For both activation and inhibition of the RhoA/ROCK pathway, morphogenesis was enhanced over all stiffnesses with ML7, and inhibited with LPA (Fig. S7), suggesting that this mechanism is independent of extrinsic mechanotransductive cues provided by the matrix.

Neural Tube Constructs as Model System for Exploring Early Developmental Signaling. Our neural tube construct can function as a developmental model system for exploring the role of extrinsic, developmentally relevant signals in specifying morphogenesis. Thus far, in this study, RA was used as the driving morphogen in patterning this neural tube model system. We thought to investigate here whether RA acted in a specific developmental time window, and whether other key signaling pathways known to operate at these early developmental time points influenced this process.

Having used the RA concentration reported previously for Matrigel-based cysts thus far (8), we first thought to establish whether there was a dose–response effect in our synthetic system. As for Matrigel, DV patterning was clearly established at a

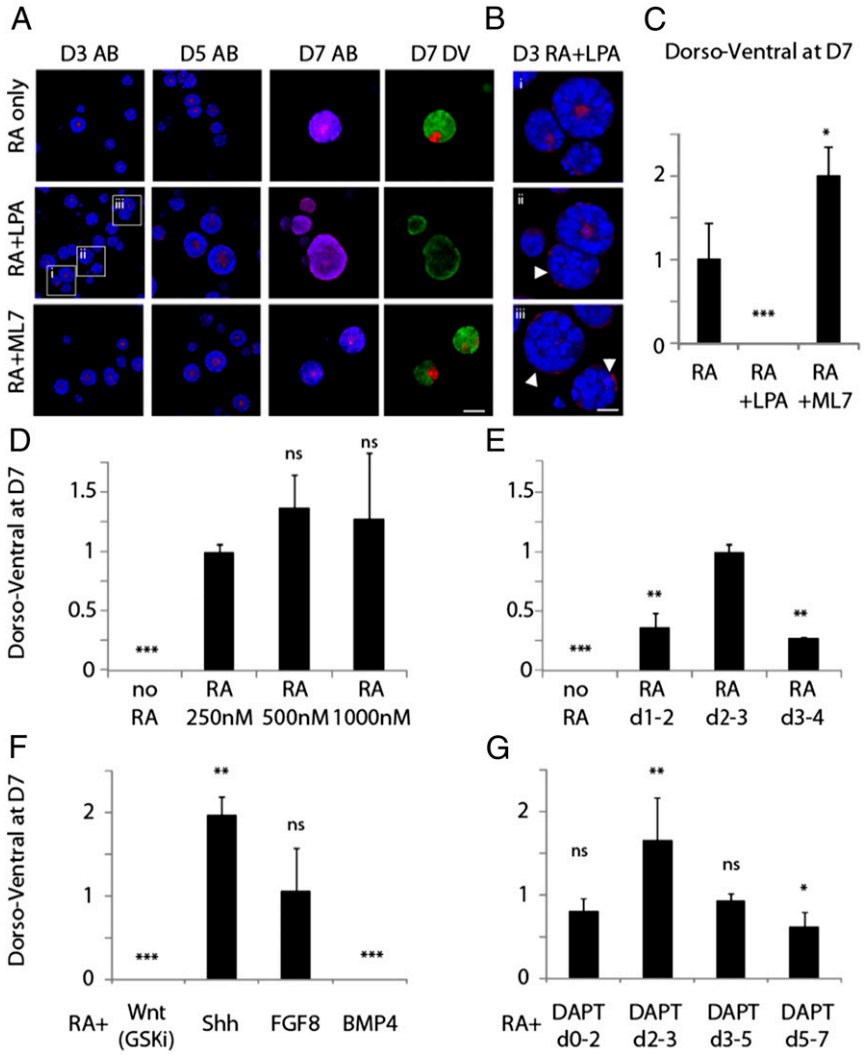

Fig. 6. Comparison of the effect of LPA and ML7 treatments on cyst apical–basal (AB) polarity at D3, D5, and D7, and on dorsal–ventral (DV) patterning at D7 (*A*), with corresponding quantification (*C*). High-magnification images of mixed polarity and inversely polarized cysts after LPA treatment at D3 (*B*). Effects of modulating RA concentration at D2–3 (*D*), modulating RA treatment time (at standard RA concentration) (*E*), developmental signaling pathway modulation at D2–3 (*F*), and Notch inhibition at various time points (*G*). All experiments in standard optimal matrix conditions (nondegradable, 2 kPa, with laminin), percentage DV efficiency corresponding to standard RA treatment (D2–3, 250 nM) set at 1, and all other treatments normalized to that of standard RA treatment (dorsoventral at D7 = % DV for treatment/% DV for standard). (Scale bars: *A*, 100 μm; *B*, 50 μm.) ***$P < 0.001$, **$P < 0.01$, *$P < 0.05$.

dose of 250 nM RA, and did not increase substantially at higher RA doses (Fig. 6*D*). Treatment with RA 1 d earlier and 1 d later substantially decreased DV patterning, confirming that colonies are competent for the morphogenetic effect of RA only in this restricted time window (Fig. 6*E*).

To begin to assess how other signaling pathways could be involved at this critical time point, we modulated the key pathways known to be involved in the establishment of the neural tube positional identity by treatment with exogenous ligands or small molecules: Shh, Wnt, BMP4, and FGF8 (22). Without RA, neither Shh, Wnt3a, BMP4, nor FGF8 alone could induce patterning, underscoring the unique role of RA at this time point for initiating a morphogenetic program. We next asked whether any of these pathways could be involved in modulating or perturbing the action of our standard RA treatment.

The exogenous addition of BMP4 completely abrogated DV patterning, as expected (Fig. 6*F*). We also observed that, although activation of the Wnt pathway via Wnt3a ligand along with RA treatment did not have a significant effect on DV patterning (Fig. S8), treatment of the downstream Wnt agonist and GSK inhibitor CHIR99021 completely suppressed DV patterning. Treatment with FGF8 did not lead to any significant effect on DV patterning (Fig. 6*F*), suggesting that RA alone is sufficient to posteriorize the cysts sufficiently to produce neural tube patterning.

RA has been shown to be required at late gastrulation stage for mesodermal and neural progenitors to respond to the Shh signal (23). Here, treatment with both RA and Shh significantly enhanced DV patterning. Intriguingly, when Shh is applied alone, no patterning is seen, or when cyclopamine, an antagonist of Shh, is applied at this time point, patterning efficiency is not significantly different to that seen in the RA-only control condition (Fig. S8) (8). This suggests that RA is the driving signal in establishing DV patterning and that Shh signal is not required for this process, but, when present, allows for higher efficiency of early symmetry-breaking events.

Finally, although the Shh, Wnt, BMP, and RA signaling pathways are well-known molecular players in neural tube patterning, we also wanted to show how this model system could be used to uncover potentially novel roles for Notch, another important player in developmental signaling. In this study, we treated our cysts with *N*-[*N*-(3,5-difluorophenacetyl)-1-alanyl]-*S*-phenylglycine

t-butyl ester (DAPT), a γ-secretase inhibitor that blocks Notch activity, at various time points, in addition to the standard RA treatment at D2–3. We observed a striking increase in DV efficiency, but only when DAPT treatment was carried out in the critical D2–3 window, together with RA (Fig. 6*G*).

Discussion

Here, we provide evidence that chemically defined microenvironments can promote the formation of complex 3D organoids that recapitulate key steps in early neurogenesis. A high-throughput materials discovery platform allowed us to systematically identify important principles in the commitment and morphogenesis of single ESC-derived colonies in a 3D context. Neuroepithelial differentiation and apical–basal polarity were generally coregulated by the same factors, whereas proliferation could be differentially modified by biophysical factors, notably by the mechanical properties of the matrix. Our analysis yielded a set of microenvironment characteristics that function together to promote proliferation, expression of Sox1, and apical–basal polarity. This approach allowed us to identify a single-compromise optimal condition, which could then be used as a benchmark in ensuing experiments. Systematic combinatorial materials screening, along with exploratory analysis based on clustering and a GLM-based analysis, provides powerful tools to begin deconstructing complex in vivo microenvironments. The determination of an optimal stiffness for apicobasal polarity in the range of 4 kPa is consistent with a recent report on MDCK cyst formation in synthetic matrices (17). Our results suggest that cell fate-specific conditions are required for the establishment of neuroepithelial polarity: for example, unlike for MDCK cysts, a nondegradable matrix is required for the establishment of polarity in the neuroepithelial context. Additionally, unlike for MDCK cysts, adhesion ligands (in our case, laminin) are required for proliferation, differentiation, and for the establishment of a lumen.

This study explicitly examines differences between Matrigel and a defined synthetic matrix in the context of stem cell-based self-organization. It becomes clear that the use of a "one-size-fits-all" ECM leads to significant heterogeneities, likely due to the presentation of conflicting or nondirected signaling, whereas synthetic matrices can function as selective and specific substrates for imposed differentiation outcomes, leading to more homogeneous and defined final populations. We postulate that a synthetic matrix does not alter the dynamics of specified differentiation and morphogenesis, but rather ensures that heterogeneous alternate morphologies and cell fates are selected out.

A number of studies have shown that a 3D environment can induce the appearance of apicobasal polarity in multicellular epithelial cell aggregates, notably in model systems such as the MDCK (24), Caco-2 (25), mammary epithelium (26), and early embryonic epiblast (27). This accumulated evidence suggests that some aspects of apical–basal morphogenesis, such as the involvement of the Rho–ROCK–Myosin pathway (28, 29), may be a conserved feature for epithelial cells. However, our study, as well as recent work with synthetic matrices involving well-known models of epithelial morphogenesis (17), suggests that, by discretely manipulating microenvironmental parameters, it is possible to uncover significant cell type-specific requirements.

Notably, we have also shown in this study how the independent manipulation of various properties of the ECM in a defined synthetic analog could yield new insights into more complex morphogenic events such as the DV patterning of a neural tube-like construct. Importantly, we provide here a link between apical–basal polarity and stem cell fate and morphogenesis. In particular, through a manipulation of matrix properties, we show that apical–basal polarity is a requirement for later morphogenic events, particularly the dorsoventral symmetry-breaking event seen in our cysts, and that the establishment of such patterning events is mediated by colony shape. We have also underscored how the dynamics of morphogenetic events are tightly regulated in time, with spatial rearrangements in 3D required for further differentiation and patterning, emphasizing that, as in in vivo development, tightly defined windows of temporal competence to specific signaling must be identified. Furthermore, the results obtained in this study, along with those seen in other model systems of epithelial polarity (24, 28, 30, 31), point to a significantly different role for actomyosin contractility in 3D compared with 2D, and underscore the need for 3D culture systems to more faithfully reproduce mechanotransduction in the context of morphogenesis. We believe that the use of our orthogonally modulatable matrix allows us to clearly demonstrate this important feature of developmental biomechanics. We have shown that, when the early epithelial apical–basal polarity is perturbed, later DV polarity cannot be initiated.

This approach demonstrates how highly tunable synthetic microenvironments can be used to elucidate the important role of biophysical factors in morphogenesis, and can offer new model systems that begin to recapitulate the complexity of in vivo developmental processes with more tractable in vitro systems.

Materials and Methods

Hydrogel Precursor Synthesis. 8arm-PEG-vinylsulfone, 40 kDa (PEG-VS) (NOF Corporation), was functionalized with FXIIIa-peptide substrates via Michael-type addition. We have used a glutamine-containing peptide (NQEQVSPL-ERCG-NH_2) and lysine-containing peptides with two MMP-sensitive sequences: AcFKGG-*GDQGIAGF*-ERCG-NH_2 (non-MMP sensitive) and AcFKGG-*VPMSMRGG*-ERCG-NH_2 (MMP sensitive). Consequently, we obtained one glutamine-PEG precursor (Q-PEG) and two lysine-PEG precursors: MMP-insensitive PEG, MMP-sensitive PEG. Functionalization and characterization of these precursors were performed as described elsewhere (14, 15). In brief, peptides were added to PEG-VS in a 1.2-fold molar excess over VS groups in 0.3 M triethanolamine (pH 8.0) at 37 °C for 2 h, followed by dialysis (Snake Skin; MWCO 10k; Pierce) against ultrapure water for 4 d at 4 °C. After dialysis, the salt-free products were lyophilized to obtain a white powder. These functionalized PEG powders were then reconstituted in water [10% (wt/vol)] to obtain working stock solutions of PEG.

Hydrogel Preparation. Factor XIII (FXIII) was reconstituted in water and activated with thrombin as described (14, 15). In brief, 1 mL of FXIII (200 U/mL) and Fibrogammin P1250 (CSL Behring) were activated in the presence of 2.5 mM $CaCl_2$ with 100 μL of thrombin (20 U/mL; Sigma-Aldrich) for 30 min at 37 °C. Aliquots of FXIIIa were stored at −80 °C for further use. Precursor solutions to give hydrogels with a final dry mass content ranging from 1% to 3% (wt/vol) were prepared by stoichiometrically balanced ([Lys]/[Gln] = 1) solutions of Q-PEG and each of the four lysine-PEGs in Tris buffer (TBS; 50 mM; pH 7.6) containing 50 mM calcium chloride. The cross-linking reaction was initiated by 10 U/mL thrombin-activated FXIII and vigorous mixing. In all nonrobotic experiments, 30-μL drops were formed on a glass coverslip dish (Mattek).

ESC Culture. Mouse feeder-independent ESCs [line 46C, Sox1-GFP knock-in (8); kindly provided by A. Smith, University of Cambridge, Cambridge, UK] were grown on gelatin-coated dishes in ESC medium: DMEM+ Glutamax (Life Technologies) basal medium supplemented with 15% (vol/vol) ESC-certified FCS (HyClone), 100 U/mL penicillin/streptomycin (Life Technologies), 1 mM sodium pyruvate (Life Technologies), 0.1 mM nonessential amino acids (Life Technologies), 0.05 mM β-mercaptoethanol (Sigma-Aldrich), and 10^3 U/mL LIF (made in-house).

Robotic Mixing and Dispensing. High-throughput combinatorial screening of 3D microenvironments was performed as described using a Hamilton Microlab StarPlus automatic liquid-handling robot with Nanopipettor head (16). All automated steps were programmed with MicroLab Vector Software, version 4.1.1 (HAMILTON Bonaduz). Stock solutions of premixed stoichiometrically balanced PEG solutions corresponding to the two peptides were prepared by mixing glutamine-PEG precursor (Q-PEG) with the two different lysine-PEG precursors: MMP-insensitive PEG and MMP-sensitive PEG. Each of these four stock solutions was diluted to the concentrations required to target stiffnesses. The dilution and all subsequent steps of the process were performed robotically, with fluid-handling parameters optimized for every material class and checked by mass measurement on a balance. Thirty percent of the total final volume was left empty (spare volume) to account for subsequent addition of proteins, cells, and FXIIIa (10% of total volume for each component).

These eight combinations (two MMP sensitivities times four stiffnesses) were aliquoted into wells of a 384-well plate. ECM proteins were thawed on ice,

diluted to a concentration of 0.5 mg/mL, and placed into the wells of a cooled 384-well plate. The proteins (including blank control) were dispensed into the 256 gel precursor-filled well, such as to obtain at the end of this step unique combinations of mechanical properties (MP), degradability (DG), and ECM proteins (EC). A 96-well plate was prepared with differentiation medium containing the soluble factor bFGF (20 ng/mL; R&D Systems) and a blank control.

The differentiation medium consisted of 1/2 vol of Neurobasal (Life Technologies), 1/2 vol of DMEM-F12 (Life Technologies), 100 U/mL penicillin/streptomycin (Life Technologies), 1 mM sodium pyruvate (Life Technologies), 0.1 mM nonessential amino acids (Life Technologies), and 0.05 mM β-mercaptoethanol (Sigma-Aldrich).

Cells were trypsinized and resuspended in serum-free medium at a concentration of 2×10^6 cells per mL and kept on ice. Simultaneously, frozen aliquots of FXIIIa were thawed and also kept on ice. Then, in a sequential fashion, cells were dispensed into eight wells of the mixed gel precursors, quickly followed by dispensing and robotic mixing of FXIIIa. Immediately following the addition of FXIIIa, and, before onset of gelation (~2–3 min), hydrogel mixtures were dispensed into a 384-well plate.

Imaging. Imaging for the high-throughput experiments was carried out on a BD Pathway 435 automated imaging system (BD Biosciences). Plates were fixed with 4% (wt/vol) paraformaldehyde and stained with DAPI and Phalloidin–Alexa 546 (1:200; Life Technologies) at D5, followed by imaging in the GFP DAPI and Alexa 546 channels. A 4× objective (Olympus UPlan FLN; N.A., 0.13) was used such that an entire well could be captured in a single field of view. At every *xy* position, that is, for every well, six images were captured across a *z*-stack height of 800 μm. For each well, these six images in each channel were collapsed into a single additive image. Imaging for time-lapse experiments in Movies S1–S8 was carried out on Zeiss Axio Observer Z1 equipped with an incubation chamber. All other imaging was performed on Zeiss confocal microscope LSM 510.

Immunohistochemistry. Immunohistochemistry was performed on fixed samples with the following antibodies and concentrations: Shh (Santa Cruz; 1:200); Pax3 (DSHB; 1:50); Nkx6.1 (DSHB; F55A10; 1:100); Olig2 (R&D; AF2418; 1:100); Isl1 (DSHB; 39.4D5; 1:100); Phalloidin-Alexa 546 (Life Technologies; 1:100); Phalloidin–Alexa 635 (Life Technologies; 1:1,000); EdU (Life Technologies; Click-iT EdU Imaging Kit); Cleaved Caspase 3 (Cell Signaling; 9661; 1:200); Brachyury (Santa Cruz; sc17745; 1:300); E-cadherin (Cell Signaling; 24E10; 1:500); N-cadherin (DSHB; MNCD2; 1:50); Laminin (Abcam; ab44941; 1:20); and Fibronectin (Santa Cruz; sc6953; 1:100).

Time-Lapse Experiments. Cells were encapsulated in PEG hydrogels and placed in the incubator for 4 hours. SiR-actin probe 32 at 1 mM was added to the cells in 1:1000 dilution (final concentration 1 μM) and cells were incubated further for 2 hours. Imaging was initiated 8 hours after initial hydrogel encapsulation.

Image Analysis. All images were processed using algorithms developed in CellProfiler, version 9777 (Broad Institute). Collapsed image stacks for each well in the GFP, DAPI, and Alexa 546 channels were input. DAPI images were thresholded and segmented. Identified colony areas in DAPI were used as masks for the GFP images. For each colony, size and fluorescence intensity measures and morphometric features such as solidity (colony area/convex hull area) and eccentricity (minor/major axes) were recorded. For each image, the number of colonies exhibiting apical–basal polarity was then semimanually recorded.

Data Processing. Matlab R2010b (MathWorks) was used to process and visually explore the data. Number of colonies, average colony area, average GFP intensity, number of colonies exhibiting apical–basal polarity, as well as solidity and eccentricity were calculated by averaging single colony data for each well and for each unique condition over triplicate wells. For hierarchical clustering, the data were centered to have mean of 0 and scaled to have SD of 1. Hierarchical clustering with Euclidean distance metric and average linkage was performed to generate the hierarchical tree.

Statistical Analysis. Data were input into R V2.14.2. GLMs that took into account all possible interaction terms were specified for analysis of colony area, GFP intensity, and percentage apical–basal polarized colonies per well. The step Akaike information criterion procedure was run to obtain optimal models based on the Akaike criterion. GLM procedure of SAS, version 9.0, software (SAS Institute) was used for compute a least-squares mean value for each factor within every category, and differences of LSmeans ± SEs with the control were tested for significance. The used models considered the effects of MP, DG, EC, and soluble factors (SF), as well as interactions determined to be significant. For all parametric tests, normality of the residues and homogeneity of the variance were examined in QQ and Tukey–Anscombe plots, respectively. For all nonrobotic experiments, data were collected from at least three biological replicates, and the two-sample *t* test with unequal variance was applied in Microsoft Excel.

ACKNOWLEDGMENTS. We thank Kai Johnsson and Lukinavicius Grazvydas for providing the live actin probe for time-lapse imaging. We thank Regina Wegner for technical assistance. This work was funded by the European Union Framework 7 HEALTH Research Programme PluriMes (https://www.plurimes.eu/); the SystemsX.ch Research, Technology, and Development Project StoNets; funding from FZ111/EXC168, Center for Regenerative Therapies Dresden; and the National Science and Engineering Research Council of Canada and Fonds de Recherche du Quebec Nature et Technologie.

1. Kojima Y, Tam OH, Tam PP (2014) Timing of developmental events in the early mouse embryo. *Semin Cell Dev Biol* 34:65–75.
2. Eyckmans J, Boudou T, Yu X, Chen CS (2011) A hitchhiker's guide to mechanobiology. *Dev Cell* 21(1):35–47.
3. Stern CD, Fraser SE (2001) Tracing the lineage of tracing cell lineages. *Nat Cell Biol* 3(9):E216–E218.
4. De Robertis EM (2006) Spemann's organizer and self-regulation in amphibian embryos. *Nat Rev Mol Cell Biol* 7(4):296–302.
5. Sato T, et al. (2009) Single Lgr5 stem cells build crypt-villus structures in vitro without a mesenchymal niche. *Nature* 459(7244):262–265.
6. Takebe T, et al. (2013) Vascularized and functional human liver from an iPSC-derived organ bud transplant. *Nature* 499(7459):481–484.
7. Lancaster MA, et al. (2013) Cerebral organoids model human brain development and microcephaly. *Nature* 501(7467):373–379.
8. Meinhardt A, et al. (2014) 3D reconstitution of the patterned neural tube from embryonic stem cells. *Stem Cell Rep* 3(6):987–999.
9. Langer R, Tirrell DA (2004) Designing materials for biology and medicine. *Nature* 428(6982):487–492.
10. Lutolf MP, Gilbert PM, Blau HM (2009) Designing materials to direct stem-cell fate. *Nature* 462(7272):433–441.
11. Griffith LG, Swartz MA (2006) Capturing complex 3D tissue physiology in vitro. *Nat Rev Mol Cell Biol* 7(3):211–224.
12. Dolatshahi-Pirouz A, et al. (2014) A combinatorial cell-laden gel microarray for inducing osteogenic differentiation of human mesenchymal stem cells. *Sci Rep* 4:3896.
13. Nii M, et al. (2013) The effects of interactive mechanical and biochemical niche signaling on osteogenic differentiation of adipose-derived stem cells using combinatorial hydrogels. *Acta Biomater* 9(3):5475–5483.
14. Ehrbar M, et al. (2007) Enzymatic formation of modular cell-instructive fibrin analogs for tissue engineering. *Biomaterials* 28(26):3856–3866.
15. Ehrbar M, et al. (2007) Biomolecular hydrogels formed and degraded via site-specific enzymatic reactions. *Biomacromolecules* 8(10):3000–3007.
16. Ranga A, et al. (2014) 3D niche microarrays for systems-level analyses of cell fate. *Nat Commun* 5:4324.
17. Enemchukwu NO, et al. (2016) Synthetic matrices reveal contributions of ECM biophysical and biochemical properties to epithelial morphogenesis. *J Cell Biol* 212(1):113–124.
18. Chung IM, et al. (2008) Bioadhesive hydrogel microenvironments to modulate epithelial morphogenesis. *Biomaterials* 29(17):2637–2645.
19. Gouti M, et al. (2014) In vitro generation of neuromesodermal progenitors reveals distinct roles for wnt signalling in the specification of spinal cord and paraxial mesoderm identity. *PLoS Biol* 12(8):e1001937.
20. Ying QL, Stavridis M, Griffiths D, Li M, Smith A (2003) Conversion of embryonic stem cells into neuroectodermal precursors in adherent monoculture. *Nat Biotechnol* 21(2):183–186.
21. Bryant DM, Mostov KE (2008) From cells to organs: Building polarized tissue. *Nat Rev Mol Cell Biol* 9(11):887–901.
22. Lippmann ES, et al. (2015) Deterministic HOX patterning in human pluripotent stem cell-derived neuroectoderm. *Stem Cell Rep* 4(4):632–644.
23. Ribes V, Le Roux I, Rhinn M, Schuhbaur B, Dollé P (2009) Early mouse caudal development relies on crosstalk between retinoic acid, Shh and Fgf signalling pathways. *Development* 136(4):665–676.
24. Zegers MM, O'Brien LE, Yu W, Datta A, Mostov KE (2003) Epithelial polarity and tubulogenesis in vitro. *Trends Cell Biol* 13(4):169–176.
25. Pereira C, Araújo F, Barrias CC, Granja PL, Sarmento B (2015) Dissecting stromal-epithelial interactions in a 3D in vitro cellularized intestinal model for permeability studies. *Biomaterials* 56:36–45.
26. Bissell MJ, Rizki A, Mian IS (2003) Tissue architecture: The ultimate regulator of breast epithelial function. *Curr Opin Cell Biol* 15(6):753–762.
27. Bedzhov I, Zernicka-Goetz M (2014) Self-organizing properties of mouse pluripotent cells initiate morphogenesis upon implantation. *Cell* 156(5):1032–1044.
28. Yu W, et al. (2008) Involvement of RhoA, ROCK I and myosin II in inverted orientation of epithelial polarity. *EMBO Rep* 9(9):923–929.
29. Priya R, et al. (2015) Feedback regulation through myosin II confers robustness on RhoA signalling at E-cadherin junctions. *Nat Cell Biol* 17(10):1282–1293.
30. Yu W, et al. (2005) Beta1-integrin orients epithelial polarity via Rac1 and laminin. *Mol Biol Cell* 16(2):433–445.
31. O'Brien LE, et al. (2001) Rac1 orientates epithelial apical polarity through effects on basolateral laminin assembly. *Nat Cell Biol* 3(9):831–838.
32. Lukinavicius G, et al. (2014) Fluorogenic probes for live-cell imaging of the cytoskeleton. *Nature Methods* 11:731–733.